Using CFD to Improve Simple Aerodynamic Models for Rotor Codes

J. Beedy, G. N. Barakos, K. J. Badcock, and B. E. Richards

Computational Fluid Dynamics Lab,

Department of Aerospace Engineering,

University of Glasgow,

Scotland G12 8QQ, United Kingdom.

Abstract

In current industrial practice, comprehensive rotor codes are used as design tools. Such codes rely on simplified representations of the aerodynamics mainly due to the industrial need for efficient calculations. High fidelity aerodynamics is also required and this requirement forms the basis of the current work. It is now accepted that one of the most powerful and promising tools available for the prediction of the loads on a rotor is Computational Fluid Dynamics (CFD) and several researchers have already employed CFD in rotorcraft simulation. Although this approach is compatible with the industrial requirement for accurate prediction of rotor loads, it is fair to say that most of the time CFD requires significant amounts of CPU time making the adoption of CFD by industry harder. In addition, most helicopter manufacturers have developed design methodologies which cannot be dropped over night and be replaced by CFD. This work aims to address these issues, and incorporate elements of CFD into the research and design of helicopter rotor blades. CFD will be mainly used to reduce the amount of experimental data required for tuning the existing aerodynamic modules used in comprehensive rotor codes. CFD will also be used to put forward suggestions for improving the models currently employed by providing a deeper understanding of the flow features encountered within the rotor blade environment with the view to addressing some of the deficiencies that have been highlighted in the aerodynamic models. The objectives of the research program are: (a) To validate the CFD code of the University of Glasgow, PMB for turbulent, unsteady flows around the tips of helicopter blades. (b) To perform parametric studies on the Reynolds and Mach numbers, the geometry of the rotor and its motion. (c) To extract understanding out of the CFD calculations and the available experiments. (d) Exploit this information to modify the currently available tools for predicting aerodynamic loads on rotors.

C_p	Pressure coeff. $\frac{1}{2\rho U_\infty^2}(P-P_0)$
k	Reduced frequency of oscillation, $\frac{\omega c}{U_\infty}$
M	Mach number
Re	Reynolds number, $\rho U_\infty c/\mu$
U	Local Axial Velocity
U_∞	Free-stream axial velocity
A	Coefficients given by Jones [1]
AR	Aspect ratio $\frac{b^2}{S}$
b	Coefficients given by Jones [1]
b	Semi-chord length $\frac{c}{2}$
C_{L_α}	Lift curve slope
CP	Centre of pressure
c	Chord length
f	Separation point $\frac{x_{sp}}{c}$
M	Mach number
s	Non-dimensional time
t	Dimensional time
T_l	Time constant (impulsive loading)
T_p	Time constant $T_p \propto M$
T_q	Time constant (impulsive loading due to pitch rate)
U	Freestream velocity
x_{ac}	Aerodynamic centre
α	Angle of incidence
$\overline{\alpha}$	Step change in angle of incidence
η	Function of sweep back angle
Λ	Sweep back angle
$\phi_c(s)$	Circulatory indicial lift function
$\phi_l(s)$	Impulsive indicial lift function
$\phi_p(s)$	Impulsive indicial lift function due to pitch rate
$\dot{\theta}$	Pitch rate about $\frac{3}{4}$ chord position
ρ	Density
τ	Vortex time $0 \leq \tau \leq T_{v_1}$
α	Incidence
α_0	Mean oscillatory incidence
α_1	Amplitude of oscillation
μ	Viscosity
ρ	Density
ρ_∞	Density at free-stream
ω	Oscillation Frequency

Presented at the AHS 4^{th} Decennial Specialist's Conference on Aeromechanics, San Francisco, California, January 21-23, 2004.

Introduction

At present, most rotorcraft design is performed using relatively simple aerodynamic models like the ONERA model [2, 3] or indicial methods like the one put forward by Beddoes [4, 5, 6]. Such models usually form part of more comprehensive tools attempting to model full rotor configurations taking into account aerodynamics as well as aeromechanics. On the other hand, experimental investigations and flow simulation using computational fluid dynamics (CFD) are often used but have a secondary role restricted to very specific parts of the rotor and centered around several flow phenomena like dynamic stall or blade vortex interaction. The first group of tools has the advantage of being more comprehensive. It lacks, however, details of the aerodynamic phenomena which may be important in the overall prediction of the rotor loads. The second category of tools is very detailed and can also be very accurate, however, it gives limited information to the design engineers. In recent years, CFD has attempted to close the gap with more and more rotor calculations appearing in the literature[7, 8, 9]. Still, the CPU time requirements prohibit CFD from being widely used within rotorcraft design. Due to this problem, engineers and researchers have looked into ways of bridging this gap by attempting to increase the fidelity of the employed aerodynamic models using experimental data and more recently CFD. Using CFD for selected flow cases pertinent to rotors and attempting to extract enough understanding to develop a reduced aerodynamic model incorporating enough physics to allow for its general use is a challenging intellectual task. Not only enough understanding of the simulated flow is required but also full confidence on the employed CFD tool.

In view of the above, the present work attempts to combine CFD results from an established solver in order to generate the required aerodynamic data for the indicial model currently in use by Westland Helicopters. The CFD solver is the Parallel Multi-Block code of the CFD laboratory at the University of Glasgow and the indicial aerodynamic model is based on the works by Beddoes[4, 5, 6]. Several steps have been taken in this direction and the results are reported in this paper. At first, the indicial model has been analysed and all necessary aerodynamic coefficients have been identified. A set of CFD calculations was then put in place in an attempt to mimic the tunnel experiments used during the development of the model. In a second step, the sensitivity of the model to each of the coefficients has been analysed. It soon become evident that the model was more sensitive to the values of certain coefficients and this sensitivity was higher in the near-tip region. In a third step the predictions of the indicial model for the forward flight of a Lynx metal blade using the original set of coefficients and the CFD generated ones has been compared. Once this was complete a further set of CFD calculations was undertaken to further validate the PMB code for tip vortex flows. This validation process used the experimental work of Chang *et al* [10] and Ramaprian *et al* [11, 12] to predict the structure and strength of the tip vortex during roll-up from oscillating wings. The results of this part of the study showed that the PMB code could accurately predict the near tip region of unsteady flows, and could then used with confidence for tuning the reduced models.

Employed Simulation Tools

CFD Solver

The CFD solver used for this study is the PMB code developed at the University of Glasgow [13]. The code is capable of solving flow conditions from inviscid to laminar to fully turbulent using the Reynolds Averaged Navier-Stokes (RANS) equations in three dimensions. These equations are non-dimensionalised and transformed from a Cartesian reference system to a curvilinear one before being solved. The use of the RANS form of the equations allows for fully turbulent flow conditions to be calculated with appropriate modelling of turbulence. The turbulence model used for this study is the standard $k-\omega$ model [14]. To solve the RANS equations, a multi-block grid is generated around the required geometry, and the equations are discretised using the cell-centered finite volume approach. Convective fluxes are discretised using Osher's upwind scheme, which is used because of its robustness, accuracy and stability properties. Viscous fluxes are discretised using central differences. Boundary conditions are set using sets of halo cells. The solution is marched implicitly in time using a second-order scheme and the final system of algebraic equations is solved using a conjugate gradient method.

Reduced Model

The reduced aerodynamic model employed for this work is currently in practice with Westland Helicopters and is based on the aerodynamic model developed by Beddoes [4, 5, 6]. Several aspects of this model which is build on an indicial evolution of the aerodynamic coefficients of blade sections are discussed in the paragraphs.

The indicial model was aimed at calculating the unsteady aerodynamic forces encountered in helicopter rotor operating environments. The method was developed based on several criteria including simplicity to allow for quick computational times, incorporation of both attached and separated flow conditions and the ability to include arbitrary forcing functions which is necessary to adequately predict the forcing encountered within the helicopter rotor environment. In this operating environment, the aerodynamic forcing on the blades is often out of phase with the blade response, and this can result in resonance and flutter. Also the encountering of wake vortices can excite higher natural frequencies, and have the same undesired effect. The interaction between blades and vortices can also result in large changes in incidence due to the induced velocity, which can in turn cause a large increase in the lift and pitching moment, or cause the blade to stall locally.

Based on these considerations, the model assumed the form of an indicial response function for the attached flow regions. To incorporate the effects of separated flows on the blade loading, a dynamic stall model has been developed based on empirical observations of dynamic stall on aerofoil sections. These two approaches allow for the calculation of the lift and pitching moments due to variations in the incidence of aerofoil sections and the Mach number of the flow as a function of both time and azimuth angle. The model has been extended to include effects of local separation including both trailing edge and leading edge cases. Effects of planform and sweep variation have been included using a method based on the work of Küchemann [15]. These inclusions have extended the viable range of calculations.

Derivation of Indicial Lift Function

The indicial lift functions which forms the basis of this numerical model are constructed from exponential functions in time [4]. This approach allows for a simple derivation of the response using Laplacian transformations to give the lift transfer functions. Also this approach allows for the calculation of arbitrary forcing of the blades using a superposition procedure.

$$\begin{aligned} C_L(s') = C_{L\alpha}(M)\overline{\alpha}\phi_C(s') \\ +\phi_I(s')\overline{\alpha} + \phi_q(s')\overline{q} \end{aligned} \tag{1}$$

Where $C_{L\alpha}(M)$ is the lift curve slope for the corresponding Mach number, $\overline{\alpha}$ is the step change in angle of attack defined as the downwash angle at the $\frac{3}{4}c$ position, and $\overline{q}$ is the non-dimensional step change in pitch rate about the $\frac{3}{4}c$ position defined as $\frac{\dot{\theta}c}{U}$. This general form of the indicial lift response can be broken down into the lift due to the impulsive and circulatory components of the response. From (1) the circulatory component of the indicial lift function is given by:

$$\phi_C(s') = 1 - A_1 e^{(-b_1 s')} - A_2 e^{(-b_2 s')} \tag{2}$$

The impulsive loading contribution to the indicial lift response is represented by the last two terms of equation (1). Firstly, the general impulsive component of (1) is given by:

$$\phi_I(s') = \frac{4}{M} e^{(\frac{-s'}{T_I'})} \tag{3}$$

Secondly, the impulsive loading due to the pitch rate about $\frac{3}{4}c$ is:

$$\phi_q(s') = \frac{-1}{M} e^{(\frac{-s'}{T_q'})} \tag{4}$$

Attached Flow Model

Due to the nature of helicopter rotor aerodynamics, there is a requirement to incorporate both harmonic forcing functions and arbitrary forcing functions into the calculations of rotor loads To incorporate these effects, the indicial approach is used to calculate the harmonic forcing terms for the attached flow regions. A Wagner Function [1] modified for compressibility is used for this purpose. The function is derived from the impulsive increase in circulation about the aerofoil due to an infinitesimal change in the angle of attack. With the impulsive motion starting from the origin (i.e. when $s = 0$) there is a downwash flow due to the tangential nature of the flow to the aerofoil. This is given by $w = Usin\alpha \doteq U\alpha$. Assuming that there is a finite velocity at the trailing edge, the circulatory lift is given by:

$$\begin{aligned} L &= 2\pi b\rho U w\phi(s) = 2\pi\frac{c}{2}\rho UU\alpha\phi(s) \\ &= (2\pi\alpha)\left(\frac{c}{2}\rho U^2\right)\phi(s) \end{aligned} \tag{5}$$

where

$$\phi(s) = 0 \text{ if } s < 0,\, s = \frac{Ut}{b} \tag{6}$$

This function can not be used for the calculation of lift in the current form due to the nature of the helicopter operating environments. To allow this function to be applied, it must be approximated to include the constant variations in incidence encountered around the azimuth, and also the compressibility encountered at the rotor tip during high speed flight. The Wagner function is:

$$\phi_c(s) = 1 - A_1 e^{-b_1 s} - A_2 e^{-b_2 s} \tag{7}$$

where the A_i and b_i coefficients are given in [1] such that:

$$\phi_c(s) = 1 - 0.165 e^{-0.0455 s} - 0.335 e^{-0.30 s} \tag{8}$$

The modification of the Wagner function for compressibility uses the Prandtl-Glauert [16] transformation approach which results in a modified function:

$$\phi_c(s') = \frac{\phi_c(s)}{\sqrt{1-M^2}} \tag{9}$$

Using the above modified Wagner function, the lift due to harmonic variations in the incidence of the aerofoil section can be calculated. This is done using equation (5) as follows:

$$C_L = C_{L_\alpha}(M)\Delta\alpha\phi_c(s) \tag{10}$$

since

$$C_L = \left(\frac{L}{\frac{1}{2}\rho c U^2}\right) \tag{11}$$

To incorporate the harmonic and arbitrary forcing terms, it is necessary to use an exponential approximation to the Wagner function. This approximation also incorporates the influences of time, and hence covers the hysteresis effects encountered in dynamic systems. The lift is calculated as follows:

$$C_L = C_{L_\alpha}(M)\alpha_E(s) \tag{12}$$

Where $\alpha_E(S)$ is given in time as exponential lift decrements:

$$\alpha_E(t) = \alpha_{n=0} + \sum_1^n \left(\Delta\alpha_n - X_n - Y_n\right) \tag{13}$$

For generalised motion, the incidence is taken to be the downwash angle at the $\frac{3}{4}$ chord position where:

$$X_n = X_{n-1} e^{\frac{-2b_1 U \Delta(t)}{c}} + A_1 \Delta\alpha_n \quad (14)$$

$$Y_n = Y_{n-1} e^{\frac{-2b_2 U \Delta(t)}{c}} + A_2 \Delta\alpha_n \quad (15)$$

This approximation also allows for experimental lift curve slope values to be incorporated into the sampling process. For each sampling interval given by:

$$\Delta s' = s(1-M^2) = \frac{\Delta t(1-M^2)2U}{c} \quad (16)$$

in real time, it is possible to calculate the lift produced by the aerofoil section. The pitching moment and drag for the attached flow model are calculated by curve fitting experimental data for the relevant incidence.

This model applies only to attached flow regions of the aerofoil. For helicopter operations near the edge of the flight envelope, there are highly separated regions encountered by the rotors, and hence it is necessary to incorporate the effects of separation using a different model. Beddoes achieved this using an empirically based dynamic stall model [4].

Dynamic Stall Model

The main dependence of this model is on the static characteristics of the aerofoil sections which in turn depend on the profiles, Mach numbers and Reynolds numbers of the flow conditions. The boundary between the attached flow model and the dynamic stall model is defined by the separation of the boundary layer. This point is demarked by a break in the static aerofoil pitching moment curve which is defined by an incidence α_1. As separation occurs in a dynamic case, a vortex is shed from the leading edge of the pitching aerofoil, and travels chordwise along the section towards the trailing edge. As this vortex travels, the position of the centre of pressure also travels rearwards. At a second angle of attack α_2 the dynamic stall vortex is assumed to have passed over the trailing edge, the centre of pressure restablises, and the lift begins to diverge. From the analysis of experimental data, two time delays demarking firstly the onset of pitching moment, and secondly the onset of lift divergence have been observed. These time delays are essentially independent of the frequency or amplitude of the harmonic oscillations, aerofoil profile, or flow conditions.

Application of dynamic Stall Model

The approach that the model takes in calculating the lift and pitching moment during dynamic stall of the aerofoil is as follows:

- As the incidence α increases above α_1, the dynamic stall model is employed.
- For a time τ_1 after the static pitching moment break, the lift and pitching moment are calculated as for the attached flow model.
- After τ_1, it is assumed that a vortex is shed from the leading edge.
- For a time period τ_2 during which the vortex traverses the chord of the aerofoil, the lift is calculated as for the attached flow model, but the pitching moment diverges, as a result of the movement of the centre of pressure variation caused by the vortex.
- After this second time delay, there is a stabilisation of the centre of pressure, due to the vortex leaving the trailing edge. At this point, there is lift divergence, and a process of reattachment is initiated. This continues until such time as α is less then α_1 when lift and pitching moment are calculated as for the attached flow model.

During the vortex shedding, the centre of pressure is calculated as a function of incidence and time. The representation of the centre of pressure travel is the exponential response to a step change in C_P, and is implemented in the same manner as the Attached Flow model. The implementation of this movement of the centre of pressure allows the blending between the positions of the centre of pressure for attached flow conditions and separated flow conditions.

Separation leading to Dynamic Stall

Two basic mechanisms of separation were considered in the present indicial model. Firstly, the stall resulting from the progressive separation of the boundary layer from the trailing which gives relatively gradual stall characteristics. Secondly, stall resulting from separation of the boundary layer at the leading edge due to separation bubbles failing to reattach which has rapid stall characteristics. Leading edge stall characteristics are reproduced efficiently with the dynamic stall model, but the trailing edge stall is less well predicted.

Trailing Edge Separation

Trailing edge separation is the gradual separation of the boundary layer from the surface of the aerofoil from the trailing edge forwards. This form of separation is gradual in terms of the effect on the lift and pitching moment, and possesses no hysteresis effects [17]. The effect of trailing edge separation causes a loss of circulation which introduces non-linearities into the lift and pitching moments, and also causes a delay to the onset of critical conditions at high incidences. The analytical methods used to incorporate the effects of trailing edge separation into this model are based on the work of Kirchhoff [18].

These formulations for forces and moments resulting from the position of the separation point can be extended to cover the effects of trailing edge separation in dynamic flow conditions. From empirical observations of dynamic conditions, it was found that there was a lag between the forward progression of the reversal point, and the static variation with incidence [5].

Critical Pressure Rise

The effects of supercritical flow are incorporated into the model using a pressure criterion based on the shock motion. As the surface flow velocity exceeds the speed of sound, the supersonic region forming on the surface is terminated by a shock wave. As the flow increases in velocity, this region of supersonic flow increases in size, and the terminating shock moves towards the trailing edge. Eventually, the position of the shock will be such that the boundary layer will separate momentarily, and reattach forming a separation bubble. This bubble will increase in size with increasing velocity, and eventually will not be able to reattach, thus resulting in complete separation. Dynamic stall is initiated when this occurs, and this is where the pressure criterion is defined. As separation occurs, the position of the shock moves towards the leading edge under static conditions, and there is a break in the pitching moment, and lift divergence. At this point, the pressure rise across the shock is the criterion at which the dynamic stall process is applied, and the model is used to calculate the resulting lift and pitching moments.

This critical pressure rise criterion can be used for both static and dynamic flow conditions [5].

Application of the Critical Pressure Rise

To be able to use the critical pressure rise across the shock as a criterion for finding the pitching moment break defining the dynamic stall region, it is necessary to know the pressure just prior to the shock, and a relationship between the pressure and the normal force C_N. From experimental results, it was found that the phase lag in leading edge pressure with respect to the normal force coefficient is linear, with a time delay equivalent to 1.7 semi-chordlengths of travel. As this relationship is linear, it is possible to relate the pressure as a function of time $P(t)$ and the normal force coefficient as a function of time $C_N(t)$ to the static behaviour. To avoid calculating the pressures on the surface, it is possible to relate the effects in the changes in pressure to the changes in normal force coefficient. This relationship produces a new normal coefficient C'_N which may be related directly to the variation in pressure and vice versa. Thus from experimental data, it is possible to find this critical normal coefficient which directly relates to the critical pressure rise across the shock the appropriate Mach number. Using a simple transfer function, the values of C_N and C'_N may be calculated:

$$\frac{C'_N(p)}{C_N(p)} = \frac{1}{1+T_p p} \tag{17}$$

Where T_p is the time constant equivalent to 1.7 semi chordlengths of travel at a Mach number of 0.3.

This linear relationship is only applicable at low Mach numbers. At higher Mach numbers it becomes non-linear, but the same approach is still appropriate. It was found that the only variation for higher Mach numbers is the value of the time constant. This criterion is useful for both leading edge separation, and shock induced separation.

Deep Stall and Vortex Shedding

Another phenomenon that occurs during dynamic conditions is stall vortex shedding [4, 5]. As the separation point traverses the chord length, vorticity may be assumed to be shed locally, and convected downstream in the shear layers. When the point is reached that leading edge, or shock induced separation becomes dominant, there is an abrupt change in the location of the separation point, and significant vorticity will be shed in the vicinity of the leading edge. This vorticity will be convected downstream over the upper surface, and in the process cause a large variation in lift. Also, due to the location of the additional lift of the vortex, there will be a large variation in the pitching moment particularly when the vortex leaves the trailing edge.

The vortex lift is calculated as for the lift due to trailing edge separation. Using the Kirchhoff approximation for circulatory lift, the corresponding lift is given by:

$$C_{V_n} = C_{NV_n}\left(1 - K_{N_n}\right) \tag{18}$$

Where

$$K_{N_n} = \frac{1}{4}\left(1+\sqrt{f}\right)^{\frac{1}{2}} \tag{19}$$

The total vortex lift, C_{NV}, is allowed to decay exponentially with time, but may be updated by a new increment in lift:

$$C_{NV_n} = C_{NV_{n-1}} E_V + \left(C_{V_n} - C_{V_{n-1}}\right) E_V{}^{\frac{1}{2}} \tag{20}$$

Where:

$$E_V = e^{\left(\frac{\Delta t}{T_V}\frac{2U}{c}\right)} \tag{21}$$

Thus when the rate of change of lift is low, the vortex lift is being dissipated as fast as it builds up. When the leading edge of pressure rise criterion applies abruptly, there is an rapid build up of vorticity, and this is convected downstream. The rate at which this is convected is determined experimentally. This experimental behaviour has been modelled as:

$$CP_V = \frac{1}{4}\left[1+\sin\pi\left(\frac{\tau_V}{T_{V_1}} - \frac{1}{2}\right)\right] \tag{22}$$

Where the vortex time $\tau_V = 0$ at the point of vortex shedding from the leading edge, and $\tau_V = T_{V_1}$ when the vortex passes the trailing edge. Thus the change in pitching moment due to vortex lift is given by:

$$C_{MV_n} = CP_V C_{NV_n} \tag{23}$$

The vortex decay constant, T_V (eqn. 21), and the centre of pressure travel constant, T_{V_1} are evaluated from experimental data.

Sweep Effects and Separation Points

The model outlined so far is based on strip theory. This method is suitable for mid-sections of rotors away from the effects of the tip region, but takes no account of the effects of planform changes such as swept rotor tips, or BERP tip planforms. Using a modified method developed by Küchemann [15] to analyse wing sweep and tip effects, it is possible to calculate the loading of a rotor blade of arbitrary planform [19]. The original method aimed to modify the lift curve slope using a value derived from the lift achieved at the centre of a doubly infinite swept back wing. From this, a lifting line method was used to find the spanwise lift distribution including the effects of locally induced downwash. For a doubly infinite swept back wing (Λ) the local sectional lift curve slope is given by:

$$C_{L_\alpha} = 2\pi\eta \frac{\cos\Lambda}{\sin\left(\frac{\pi\eta}{2}\right)} \tag{24}$$

where

$$\eta = \left(1 - \frac{\Lambda}{\pi/2}\right) \tag{25}$$

The spanwise variation was achieved by making η a function of the absolute distance y. This also modifies the aerodynamic centre:

$$\eta(y) = \left(1 - \phi(y)\frac{\Lambda}{\pi/2}\right) \tag{26}$$

where

$$\phi(y) = \left(1 + \left(\frac{2\pi y}{c}\right)^2\right)^{\frac{1}{2}} - \frac{2\pi y}{c} \tag{27}$$

The aerodynamic centre as a function of y is given by:

$$\frac{x_{ac}}{c} = \frac{1}{2}\left(1 - \frac{\eta(y)}{2}\right) \tag{28}$$

From these equations, it is possible to calculate the effects of sweep on the lift generated by the rotor sections. To include the effects of the tip, the above equations are used but with the sign of the sweep angle reversed. Thus between these sections, the lift is simply the sum of these two contributions. During the original development of this method, it was found that for low aspect ratio wings, this method was not applicable. To overcome this problem when considering closely spaced discontinuities in planform it is desirable to minimise the value of $\eta(y)$ as the panel aspect ratio tends to 0. Thus a factor similar to the first order lift curve slope correction is used to eliminate this problem:

$$\eta'(y) = \eta(y)\frac{AR}{1+AR} \tag{29}$$

With the above equations, it is possible to calculate the effects of arbitrary planforms on the forces and moments generated by the rotor blades.

Wake Modelling

The loads experienced by the rotor blades are not only due to the local flow conditions, but also affected by the wake produced by the preceding blades. The effect of the wake is to alter the local incidence experienced by the blades, and often this alteration is rapid, i.e. the interaction of the blades with tip vortices shed by the previous blades. This leads to large variations in the local incidence, and rapid changes in the local lift experienced by the blade. To include the effects of the wake in the rotor code, the method of wake prediction must be compatible with the indicial model for unsteady aerodynamic loading response already outlined in the previous sections. The influence of time varying shed wake is included implicitly in the model outlined previously, but the effects of tip vortices needs to be included explicitly, and this is where the wake model is used. The standard approach is to keep track of all the individual vortex elements along with the geometry of the wake, and sum the individual contributions from each element. Unfortunately, this method may be too lengthy and would require excessive computational time. To avoid this problem, an approximation is made. Firstly, the model is divided into two sections, the near wake model and the far wake model. The near wake model covers the first quadrant of the vortex life, and from then the far wake model is used to calculate the influence on the downwash induced by the vortices [20, 21]. Beyond the first quadrant, the vortex is assumed to be rolled up, and hence can be treated as a single tip vortex. The approach taken by Beddoes [20] for resolving the wake influences, while maintaining the simplicity and efficiency of the model, uses a "free wake" method to calculate the mutual distortion and induced velocities of the trailing and shed elements of the wake. The distortion of the wake is achieved by using a prescribed downwash field which is time averaged. Using this distorted wake, the local induced velocity on the blades can be evaluated by dividing the vortex trails into a series of elements, and applying the Biot Savart Law. To avoid the excessive computational costs of evaluating every element of the vortex trail for several turns of the rotor, an approximate method is used. This method identifies the most critical points of the wake, and at these points positions large vortex elements, and approximates the influence of the remaining wake elements by using a vortex ring element.

CFD Calculations

Due to the complexity of the model a summary of its aerodynamic coefficients is presented in Table 1. As can be seen the model needs 19 coefficients obtained for each blade section and for each Mach number. In practice 14 different values of the Mach number are used between 0.3 and 0.95.

Estimating Model's Coefficients

To generate the coefficients required for the Beddoes model, a number of flow cases must be calculated for the different aerofoils used in each blade. These include both quasi-steady ramping cases for the attached flow portion of the model, and oscillatory cases for the dynamic stall portion. To generate the steady coefficients in an efficient manner for each aerofoil, a quasi-steady calculation procedure is used. This is in the form of an unsteady calculation at each Mach number within the required range. A ramping motion at a very low pitch rate is applied to each section to allow the coefficients outlined in Table 1 to be calculated from the CFD results.

To calculate the constants for the dynamic stall part of the model, a number of oscillatory cases are required. These include cases with a mean incidence of oscillation below the stall angle and will give the hysteresis constants used by the current generation model. A second set of cases will cover a range of incidences over the static stall angle, and will give the constants required for the dynamic stall model, including the dynamic stall vortex convection time. Table 1 outlines the coefficients to be calculated from the CFD results for the dynamic stall part of the current model.

Results and Discussion

Having established a procedure for calculating the aerodynamic coefficients of the indicial model several comparisons are put forward. The rotor blade considered is the Lynx metal blade due to its very simple design. For this case a set of data for the indicial model was generated using some tunnel tests results at low Mach numbers and extrapolating the coefficients of the model in the transonic regime. This set of data which will be referred to as "experimental" is compared against a separate set obtained using CFD. Having two sets of coefficients for the indicial model further calculations will be attempted for the Lynx metal blade in forward flight. Finally the sensitivity of the model to the coefficients will be assessed.

Comparison between aerodynamic coefficients obtained using CFD and experiments

The Lynx metal blade is an ideal first case for exercising the procedure outlined in the previous paragraphs. The blade is made out of 3 sections; RAE9618 at the root, RAE9615 at 85% span, and RAE9617 at the tip. A linear twist of 12 degrees is applied to the blade. For simplicity, and due to the fact that the employed sections have similar aerodynamic characteristics only the RAE9615 section was used when the constants of the model were calculated from tunnel tests or classic aerodynamic theory. Using CFD, each section can be considered individually with a small cost it terms of the CPU time required for the calculations outlined in Table 1.

The PMB solver was used for all calculations and each of the coefficients has been estimated from the CFD output. Figure 1 presents the comparison for the liftslope (a), stall angle (b), static moment (c) at the zero lift angle, and drag (d) at the zero lift angle. On the same plots, data from tunnel testing and classic aerodynamics are also presented. It is already obvious from this figure that CFD allows for a better representation of the aerodynamics at high Mach numbers where testing is expensive or not available. In fact, Figure 1 (a) shows what the Prandtl-Glauert extrapolation for the lift slope has been used since no tunnel data was available. The same is true for the results presented in Figure 1 (d) where the increase of drag with Mach number is only predicted by the CFD results. Again due to lack of test data at high Mach numbers the drag has been extrapolated. One can see that overall, the CFD is in good agreement with the experimental set of data at low Mach numbers but discrepancies are obvious in the low and high transonic flow regime.

Comparison between rotor loads at forward flight obtained using CFD and experiments

Once a set of coefficients has been obtained using CFD the indicial model was exercised with the "experimental" and the CFD sets for forward flight cases. Two cases have been selected at 70kts and 130kts both for a straight and level flight. For each case the lift drag and moment predictions around the azimuth are compared at three different sections along the span of the blade along with the carpet plot of the integral blade loads. The results for the 70kts case are presented in Figure 2. These results suggest that there are some differences between the results obtained using the two sets of constants which was not surprising given the results presented in the previous paragraph. It is also interesting that better agreement between the two sets of coefficients is obtained for the section located in the mid-span of the blade. Figure 2 suggests that the integral loads vary little around the azimuth due to the moderate forward speed. Figure 3 presents similar results for the 130kt case. Although the agreement in model's predictions is not good between the two sets of constants, the qualitative characteristics of the variations around the azimuth are present, including the effect of an extended reversed flow region on the retreating blade. From this first sets of results one cannot fail to notice that large variations of the loads occur near the tip of the blade and the discrepancies between the predictions obtained with the two sets increase as the tip is approached.

Sensitivity of the model to each coefficient

In an attempt to establish the level of confidence necessary for each coefficient of the model a sensitivity study has been performed where each of the coefficients was varied by 10% plus or minus. The most sensitive coefficients were selected and results are presented in Figure 4 to 7. For all cases several sections along the span of the blade have been selected.

Figure 4 presents the sensitivity of the predicted C_L coefficient on the liftslope for 4 stations along the blade and for all azimuth angles. As shown, the results become more sensitive as the tip of the blade is approached with the worst case shown in Figure 4(d). Moving from C_L to C_M a similar picture is obtained and as shown in Figure 5 the moment coefficient is more sensitive inboards with the worst case appearing at station 18. Figure 6 shows the drag coefficient which follows, more or less, the trend of the C_L with the highest sensitivity appearing near station 26. Since drag is difficult to measure in tunnels the sensitivity of the drag coefficient was further investigated and Figure 7 shows the effect of parameter η (Table 1). Again as the tip is approached the predictions of the indicial model become more sensitive to the aerodynamic coefficient. It has to be mentioned that Figures 4, 5, 6 and 7 present the results for the most sensitive of the coefficients necessary for the indicial method. Due to the increased sensitivity of the model in the near-tip region a set of validation cases has been attempted using the PMB solver. Results are presented in the next sections.

Validation Cases for Near Tip Flow

Although several experimental and computational investigations [22, 23, 24, 25, 26] exist for flows over oscillating aerofoils and wings very few cases are suitable for this study. This is because most of the experiments focus on measuring surface pressure distributions while quantitative measurements of the wake and the tip vortices behind the wing are very rare. The first test case is based on the experiments of Chang *et al.* [10]. These oscillatory experiments were conducted in a closed-circuit wind tunnel, using a square NACA 0012 profile wing section. The flow conditions are entirely laminar which means there is no requirement for a turbulence modelling, thus making this case ideal for the initial validation of the PMB code.

The second test case is based on the work of Ramaprian *et al.* [11, 12]. The experiments consider the flow around both steady and oscillating wings, with the aim of studying the evolution of the tip vortex from a square NACA 0015 wing section.

A summary of the test cases is presented in Tables 2, and 3. Amongst many experimental investigations these appear to be the most comprehensive in terms of the measured flow field quantities, and therefore, are the most suitable for CFD validation.

Laminar Test Cases

For the laminar case (Case 1 of Table 3), experimental data are only available for oscillating wing cases. The flow conditions were set the same as for the experimental case. The experimental and computational results are presented in Figures 8, and 9. Contours are shown for the non-dimensional axial velocity $\left(\frac{U}{U_\infty}\right)$ behind the wing at two different distances ($x/c = 0.5$ and $x/c = 1.5$) and for an incidence of $\alpha = 11$ *deg.* during the pitch-up and pitch-down parts of the oscillation cycle. For all the CFD results presented, contours have been drawn between the limits indicated by the experiments, and the same number of contours is used to ensure as accurate a comparison between the results as possible. For all cases the vortex core is predicted to be close to the experimental location. On the same figures the relative position of the wing is also presented. The obtained results suggest that the tip vortex follows the motion of the wing in phase with the imposed oscillation. The dissipation of the numerical scheme was found to have little influence up to a distance of 5 chords behind the wing where the employed grid was indeed too coarse to preserve the strength of the vortex. Overall, the numerical predictions were found to agree remarkably well with the measurements apart from the region very close to the vortex core. On the other hand, the accuracy of the LDV measurements in this region is also limited due to the difficulty in accurately locating the core and measuring in a relatively slow flow.

Turbulent Test Cases

For the turbulent cases (Cases 2 and 3 from Table 3), both steady and unsteady results are included. For the steady case, the flow conditions used for computations are set to those of the experiments of Ramaprian *et al.* [11] as outlined earlier. For the unsteady case the incidence varied harmonically as reported in [12].

The steady flow case (Figures 10, and 11) shows the tip vortex at four stations rear-wards from the trailing edge. The stations correspond to distances from the trailing edge tip As was the case for the laminar predictions, the CFD results are in fair agreement with the experiments as far as the strength of the vortex, and its position are concerned. A grid of about 2 million points was used for this case, since we had to resolve in detail the turbulent boundary layers on the wing as well as the near-tip flow region. The CPU time required for this was about 3830 CPU minutes and calculation were performed on a 12-node Beowulf cluster of Athlon processors.

For the unsteady flow case (Case 3 of Table 3), results are presented in Figures 12, and 13. Contours of the non-dimensionalised axial velocity $\left(\frac{U}{U_\infty}\right)$ are presented for four time instances corresponding to incidences of 5 deg and 10 deg (Figure 12) during the up-stroke, and 15 deg and 10 deg (Figure 13) during the down-stroke. The CFD plots (Figures 12, 13) were selected to match the conditions of the figures published in [12] which are also shown here for comparison. For all plots the vortex structure is presented at a distance of $x/c = 0.67$ behind the trailing edge, and the trailing edge position is represented by the dashed line in all cases. All figures include the maximum and minimum non-dimensional axial velocity for each point in the oscillation cycle. The relative position of the vortex with respect to the wing is well predicted and the same is true for the overall shape of the vortex. This is a very encouraging result given the complexity of this unsteady flow.

Flow Fields

To understand the effect of the presence of the tip vortex on the loading of the wing, and number of plots have been included for both cases. Figure 14 presents CFD results for the C_p coefficient near the tip. Results are shown for three incidence angles during the oscillation cycle. As the wing passed from zero incidence (Figure 14(a)) a minimal disturbance on the C_p is observed. The situation changes slightly at an incidence of 15 deg. (Figure 14(c)) where a second peak of the C_p emerges near the downstream corner of the wing. This second peak is lower than the suction peak which dominates the leading edge region of the wing. An almost elliptical decay of the C_p is observed as we move from the root the tip of the wing. Finally, Figure 14(e) shows the variation at the maximum incidence of the cycle (30 deg.) At this incidence the C_p distribution near the leading edge suggests that stall is encountered. The effect of the vortex is again dominant near the trailing edge of the wing where a prominent suction peak is observed.

As with the laminar case, Figure 14 also presents the variation of the surface C_p with incidence for the turbulent case. Results are first presented for incidence of 5 deg. in Figure 14(b). As before the tip vortex is weak during this early stage of the oscillation and it has minimal effect on the C_p distribution. Due to the hysteresis of the flow, however, one may notice a small second peak of the C_p near the trailing edge of the wing. Figure 14(d) presents results at 10 deg. of incidence. The second peak near the trailing edge is now much stronger and is comparable in size with the suction peak near the leading edge. At this stage the tip vortex is well formed and appears to affect strongly the flow in the vicinity of the tip. At 15 deg. of incidence (Figure 14(f)) the leading edge of the tip has a much lower C_p than the trailing edge. This is expected since at this stage the vortex has reached a maximum in terms of size and strength.

Conclusions and Future Steps

A method for calculating the aerodynamic coefficients required for an indicial model was presented and a CFD solver was used to simulate the necessary wind-tunnel experiments. The results of this effort were found to agree well with the ones derived directly from experimental measurements and this highlights the important role CFD can play in the development and use of reduced aerodynamic models in rotor codes. The sensitivity of the model to all coefficients was studied and the most sensitive coefficients have been identified. Furthermore as the wing tip is approached the sensitivity of the model to the aerodynamic data increases and this motivated a separate study of tip flow. Using square blades which are close to the Lynx metal blade employed for this work CFD calculations were undertaken for the two cases where the vortex near the tip is measured. Results were found to be in good agreement with experiments. Having established confidence in the above procedure, future efforts are now directed towards modifying the model to account for the aerodynamics of complex tip shapes.

Acknowledgements

Financial support from Westland Helicopters Ltd. is gratefully acknowledged.

References

[1] Fung, Y.C. *'An Introduction to the Theory of Aeroelasticity'*. Dover Publications, Inc. New York, 2nd edition, 1993.

[2] Tran, C., & Petot, D. Semi-empirical model for the dynamic stall of aerofoils in view of application to the calculation of responses of a helicopter in forward flight. *Vertica*, 5(1):35–53, 1981.

[3] Dat, D., & Tran, C. Investigation of the stall flutter of an aerofoil with a semi-empirical model of 2-D flow. *Vertica*, 7(2):73–86, 1983.

[4] Beddoes, T.S. A synthesis of unsteady aerodynamic effects including stall hysteresis. *Vertica*, 1:113–23, 1976.

[5] Beddoes, T.S. Representation of airfoil behaviour. *Vertica*, 7(2):183–97, 1983.

[6] Beddoes, T.S. Practical computation of unsteady lift. *Vertica*, 8(1):55–71, 1984.

[7] Srinivasan, G., Baeder, J., Obayashi, S., and McCroskey, W. Flowfield of a lifting rotor in hover: A navier-stokes simulation. *AIAA Journal*, 30(10):2371–8, Oct. 1992.

[8] Srinivasan, G., Raghavan, V., Duque, E., and McCroskey, W. Flowfield analysis of modern helicopter rotors in hover by navier-stokes methods. *Journal of the American Helicopter Society*, 38(3):3–13, July 1993.

[9] Sidés, J., Pahlke, K., and Costes, M. Numerical simulation of flows around helicopters at DLR and ONERA. *Aerospace Science and Technology*, 5:35–53, 2001.

[10] Chang, J. & Park, S. Measurements in the Tip Vortex Roll-Up Region of an Oscillating Wing. *AIAA Journal, Technical Note*, 38(6):1092–95, 2000.

[11] Ramaprian, B. & Zheng, Y. Measurements in Rollup Region of the Tip Vortex from a Rectangular Wing. *AIAA Journal*, 35(12):1837–1843, 1997.

[12] Ramaprian, B. & Zheng, Y. Near Field of the Tip Vortex Behind an Oscillating Rectangular Wing. *AIAA Journal*, 36(7):1263–1269, 1998.

[13] Badcock, K., Richards, B. & Woodgate, M. Elements of computational fluid dynamics on block structured grids using implicit solvers. *Progress in Aerospace Sciences*, 36(5-6):351–92, 2000.

[14] Wilcox, D.C. Reassessment of the Scale-Determining Equation for Advanced Turbulence Models. *AIAA Journal*, 26(11):1299–1310, 1988.

[15] Küchemann, D. *The Aerodynamic Design of Aircraft*. Pergamon Press Ltd., UK, 1st edition, 1978.

[16] Kuethe, A.M., Chow, C-Y. *'Foundations of Aerodynamics'*. John Wiley and Sons, Inc. New York, 5th edition, 1998.

[17] Prouty, Raymond W. *'Helicopter Performance, Stability, and Control'*. PWS Publishers, Boston, USA, 1st edition, 1986.

[18] B. Thwaites. *Incompressible Aerodynamics*. Oxford Univ. Press, UK, 1960.

[19] Beddoes, T.S. A 3-D separation model for arbitrary planforms. In *47th. Annual Forum of the American Helicopter Society*, 1991.

[20] Beddoes, T. A wake model for high resolution airloads. In *Westland Helicopters Ltd.*, 1984.

[21] Beddoes, T. A near wake dynamic model. In *Westland Helicopters Ltd.*, 1985.

[22] Singh, P. & Uberoi, M. Experiments on Vortex Stability. *Physics of Fluids*, 19(12):1858–1863, 1976.

[23] Phillips, W. The Turbulent Trailing Vortex During Roll-Up. *Journal of Fluid Mechanics*, 105:451–467, 1981.

[24] Shekarriz, A., Fu, T., Katz, J. & Huang, T. Near-Field Behavior of a Tip Vortex. *AIAA Journal*, 31(1):112–118, 1993.

[25] Dacles–Mariani, J., Zilliac, G., Chow, J. & Bradshaw, P. Numerical/Experimental Study of a Wingtip Vortex in the Near Field. *AIAA Journal*, 33(9):1561–1568, 1995.

[26] Devenport, W., Rife, M., Liapis, S. & Follin, G. The Structure and Development of a Wing-tip Vortex. *Journal of Fluid Mechanics*, 312:67–106, 1996.

Variable	Description	CFD Test Cases
C_{L_α}	Lift curve slope.	quasi-steady
α_0	Zero lift angle.	quasi-steady
α_1	Static stall angle which is used to define the break in lift and pitching moment at stall.	quasi-steady
$\Delta\alpha_1$	Hysteresis modified α_1. Used to include lift hysteresis for quasi-static and low frequency motion.	oscillatory above static α_1
S_1	Exponent value for fitting separation parameter f prior to stall angle α_1.	quasi-steady
S_2	Exponent value for fitting separation parameter f after the onset of stall.	quasi-steady
k_0	For attached flow represents the aerodynamic center of the aerofoil.	quasi-steady
k_1	For fully separated flow, the center of pressure is given by $k_0 + k_1$.	quasi-steady
k_2	Used to include the positive pitching moment experienced at the onset of trailing edge separation.	quasi-steady
m	Used to modify k_2 to better represent pitching moment behaviour during trailing edge separation.	quasi-steady
C_{M_0}	Moment Coefficient at C_{L_0}	quasi-steady
C_{N_1}	Normal force Coefficient at time of vortex shedding. Used during dynamic stall, and used to match pitching moment break due to vortex shedding.	oscillatory above static α_1
C_{D_0}	Drag coefficient at C_{L_0} excluding skin friction and wave drag at the moment. These must be included for the correct calculation of power requirements.	quasi-steady
t_p	Pressure lag time constant used to vary value of C_N during dynamic conditions.	oscillatory above static α_1
t_f	Boundary layer response lag times for trailing edge separation. For vow values, leading edge separation is encountered, and this induces interactions with the primary stall vortex.	oscillatory above static α_1
η	Used to modify pressure distribution for varying Mach numbers.	oscillatory above static α_1
P_{V_1}	Primary dynamic stall vortex shedding time. The period of vortex from generation to passing the trailing edge.	oscillatory above static α_1
n	Exponent term to modify k_1. Affects the abruptness of the pitching moment break.	quasi-steady
f_b	Pitching moment break point. Allows flexibility in implementing the phase shift between the lift and moment characteristics at higher Mach numbers.	quasi-steady

Table 1: Coefficients required for numerical implementation of Beddoes model.

No	Test Case	Wing Geometry
(1)	Chang *et al.* [10]	rectangular planform, NACA 0012 profiles, zero twist
(2)	Ramaprian *et al.* (Steady) [11]	rectangular planform, NACA 0015 profiles, zero twist
(3)	Ramaprian *et al.* (Oscillating) [12]	rectangular planform, NACA 0015 profiles, zero twist

Table 2: Description of the wing geometry for the employed test cases.

No	Re	Mach Number	Turbulence Model	α_0 $(deg.)$	α_1 $(deg.)$	Reduced Frequency	Axis of Rotation	Grid Size
(1)	3.4×10^4	0.15	Laminar	15	15	0.09	$x/c=0.25$	$800,000$
(2)	1.8×10^5	0.15	$k-\omega$	-	-	-	$x/c=0.25$	$2,000,000$
(3)	1.8×10^5	0.15	$k-\omega$	10	5	0.10	$x/c=0.25$	$2,000,000$

Table 3: Summary of conditions for the employed test cases.

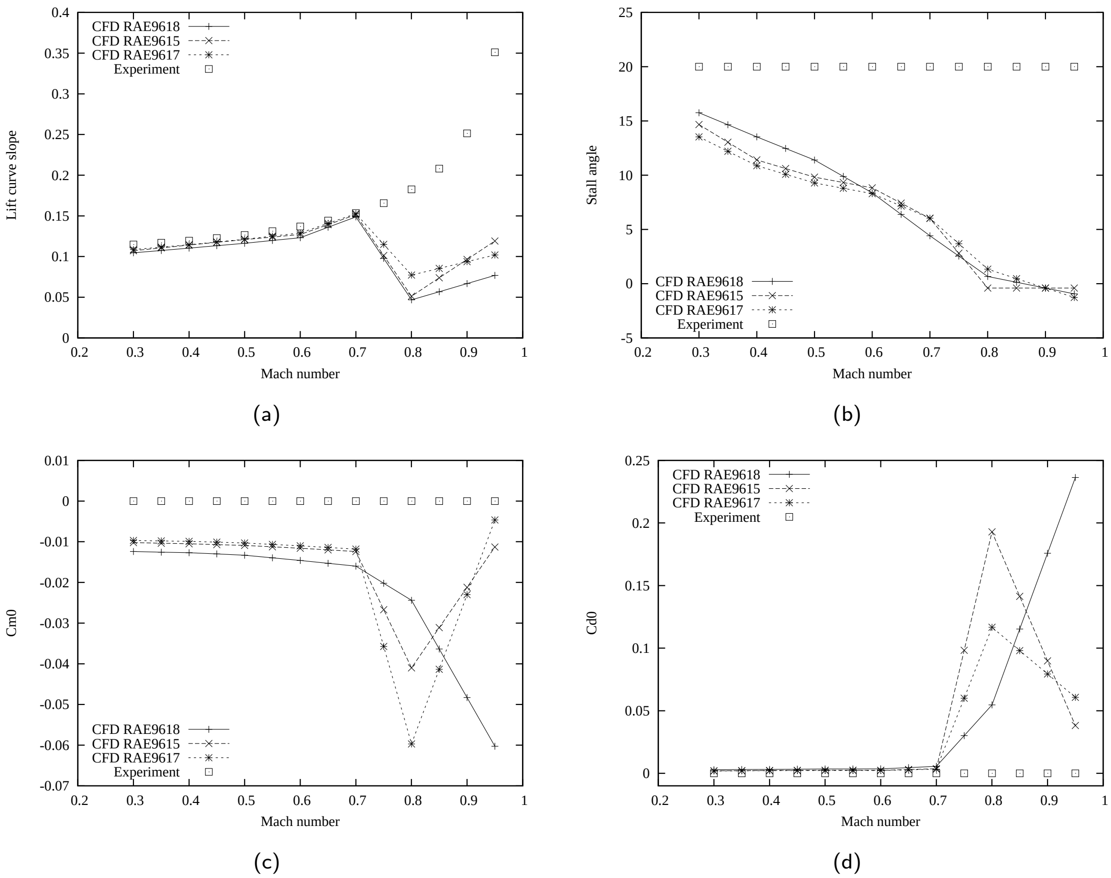

Figure 1: Comparison between experimental and CFD values for: (a) C_{L_α}, (b) α_1, (c) C_{M_0}, (d) C_{D_0}. (See Table 1)

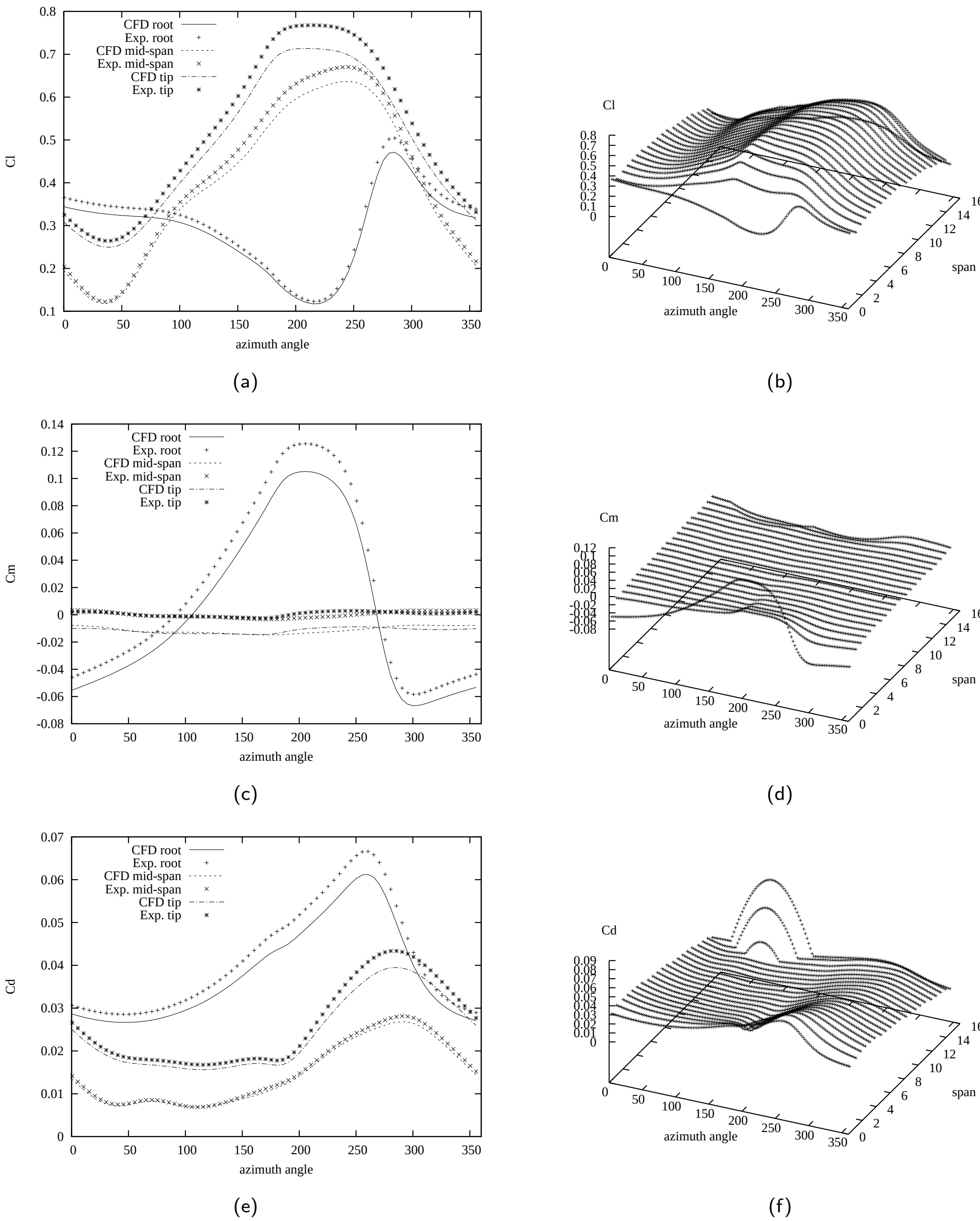

Figure 2: Lynx 70kts straight and level: (a) C_L for three spanwise locations, (b) C_L for complete blade, (c) C_M for three spanwise locations, (d) C_M for complete blade, (e) C_D for three spanwise locations, (f) C_D for complete blade.

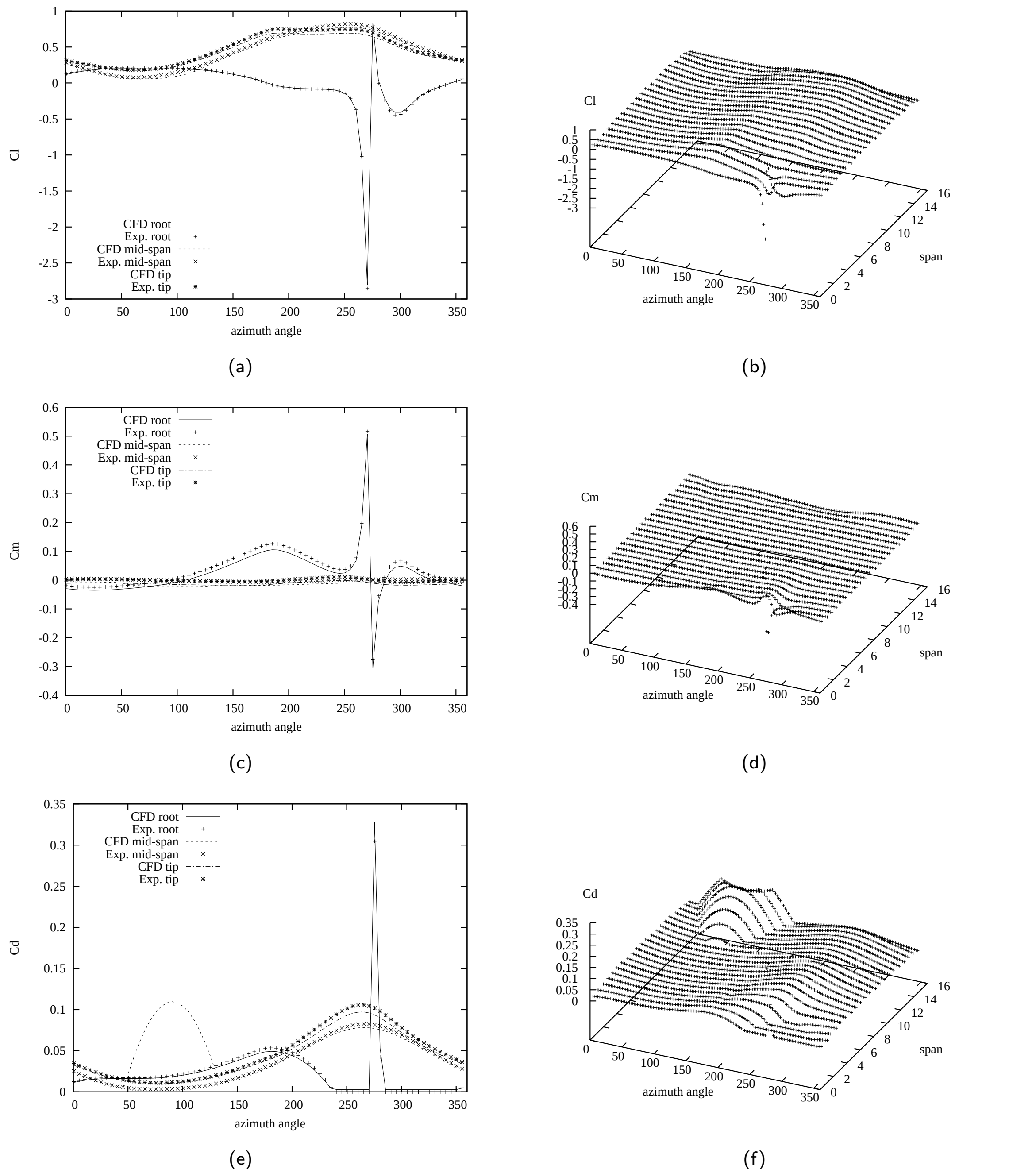

Figure 3: Lynx 130kts straight and level: (a) C_L for three spanwise locations, (b) C_L for complete blade, (c) C_M for three spanwise locations, (d) C_M for complete blade, (e) C_D for three spanwise locations, (f) C_D for complete blade.

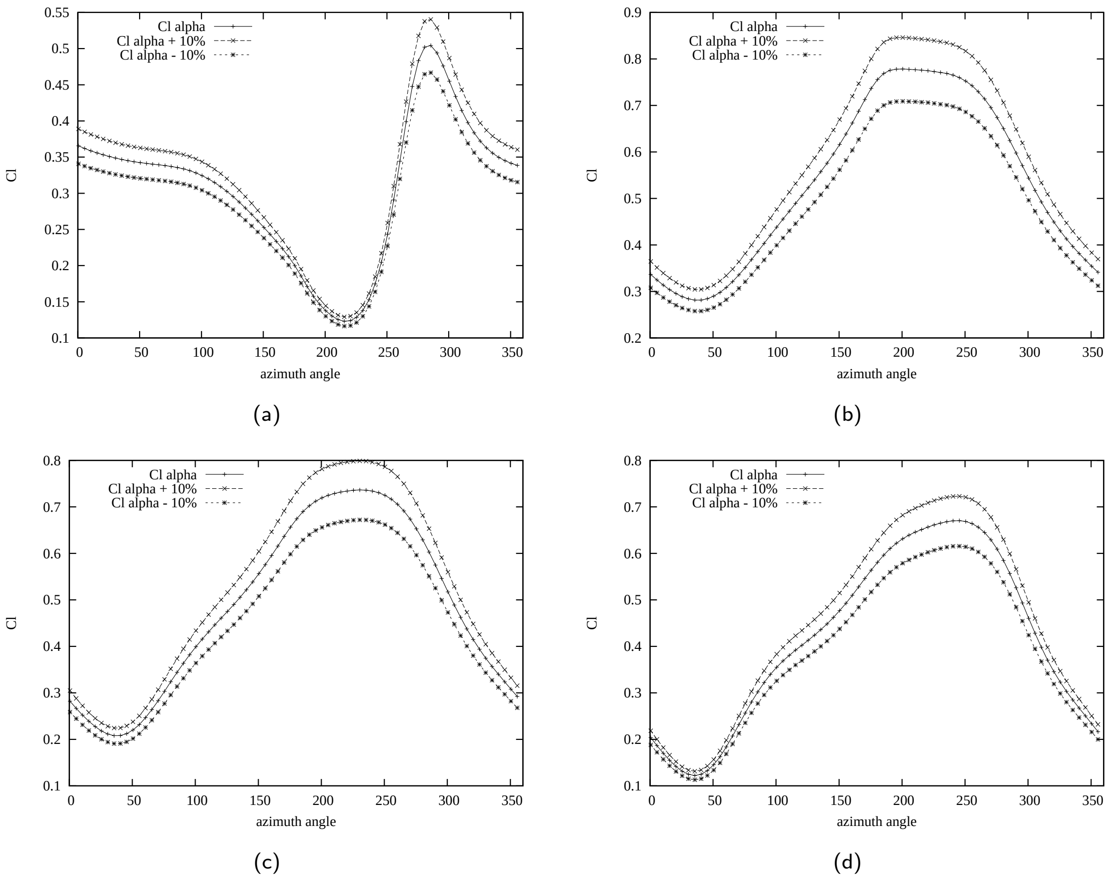

(a) (b) (c) (d)

Figure 4: Sensitivity of C_L predictions of C_{L_α} (a) for spanwise location 2 (r/R=0.28), (b) for spanwise location 18 (r/R=0.38), (c) for spanwise location 26 (r/R=0.55), (d) for spanwise location 34 (r/R=0.73). Lynx metal blade, steady level flight, 70kts.

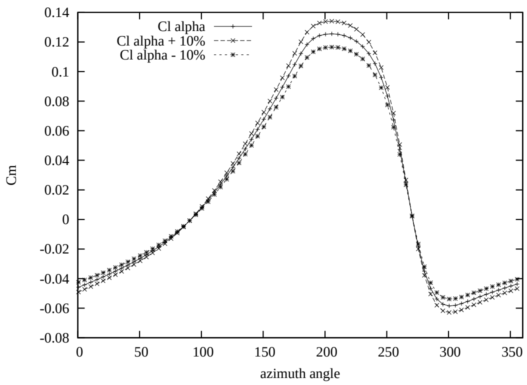

(a)

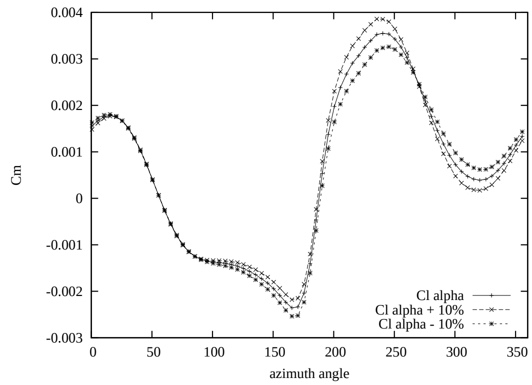

(b)

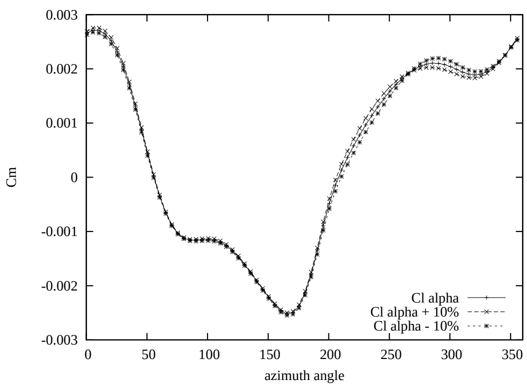

(c)

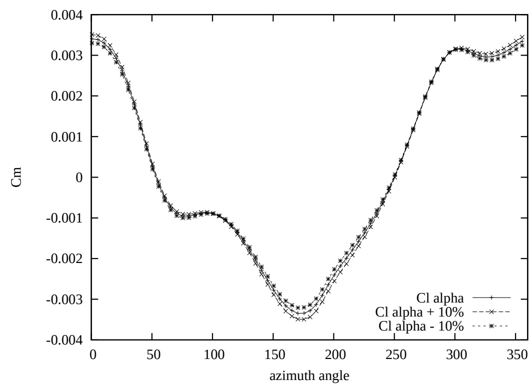

(d)

Figure 5: Sensitivity of C_M predictions of C_{L_α} (a) for spanwise location 2 (r/R=0.28), (b) for spanwise location 18 (r/R=0.38), (c) for spanwise location 26 (r/R=0.55), (d) for spanwise location 34 (r/R=0.73). Lynx metal blade, steady level flight, 70kts.

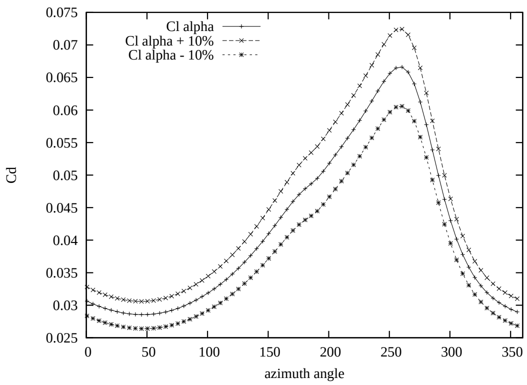

(a)

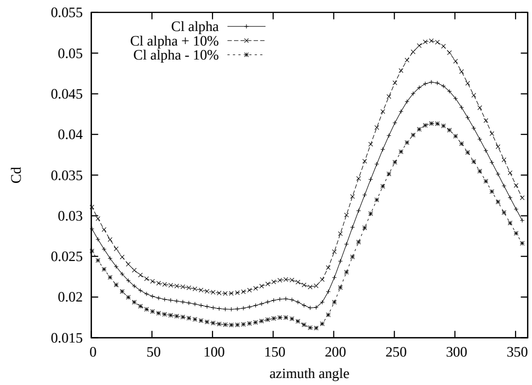

(b)

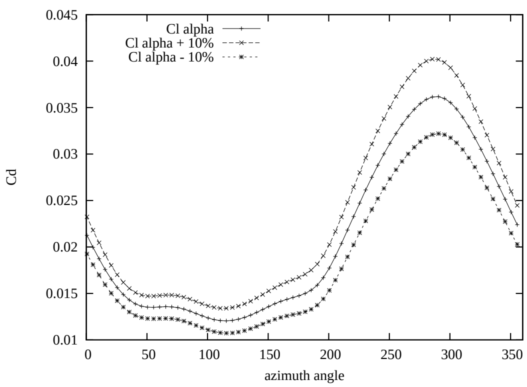

(c)

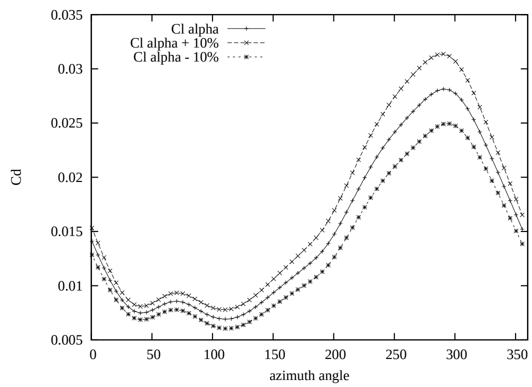

(d)

Figure 6: Sensitivity of C_D predictions of C_{L_α} (a) for spanwise location 2 (r/R=0.28), (b) for spanwise location 18 (r/R=0.38), (c) for spanwise location 26 (r/R=0.55), (d) for spanwise location 34 (r/R=0.73). Lynx metal blade, steady level flight, 70kts.

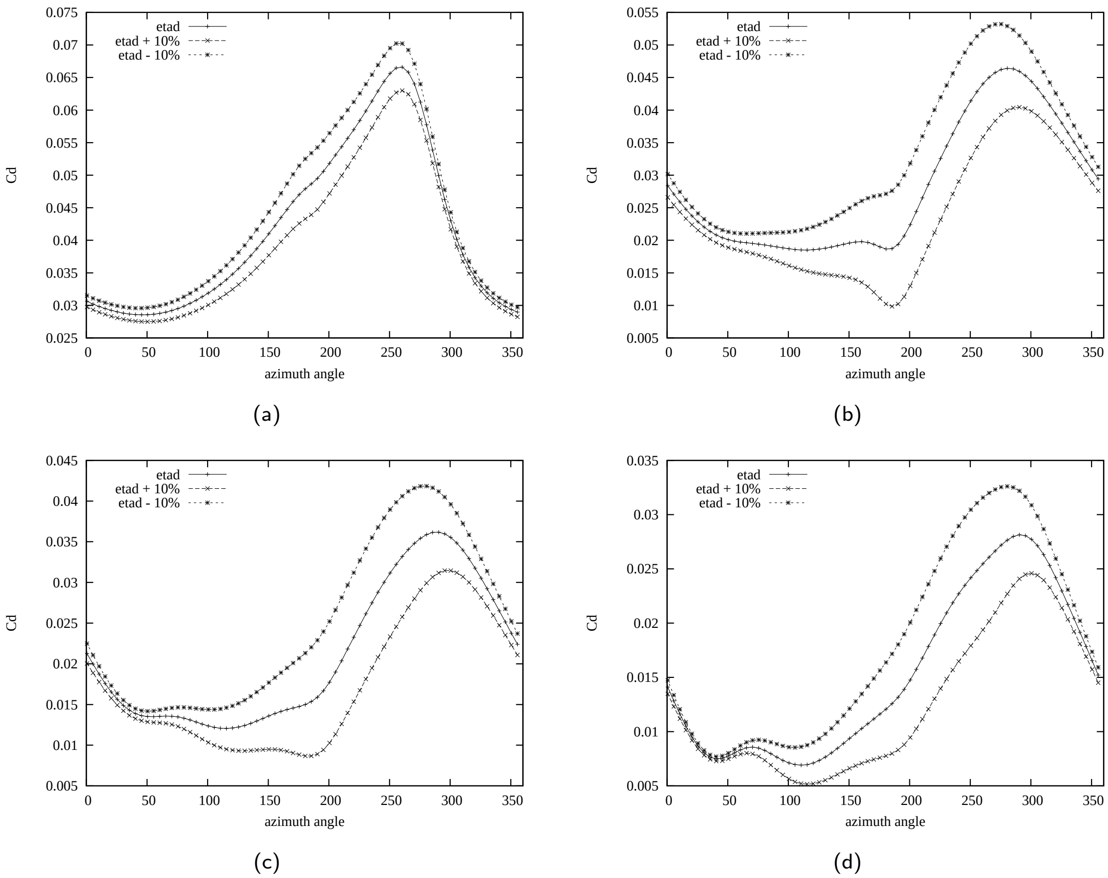

Figure 7: Sensitivity of C_D predictions of *etad* (L.E. pressure recovery efficiency). (a) for spanwise location 2 (r/R=0.28), (b) for spanwise location 18 (r/R=0.38), (c) for spanwise location 26 (r/R=0.55), (d) for spanwise location 34 (r/R=0.73). Lynx metal blade, steady level flight, 70kts.

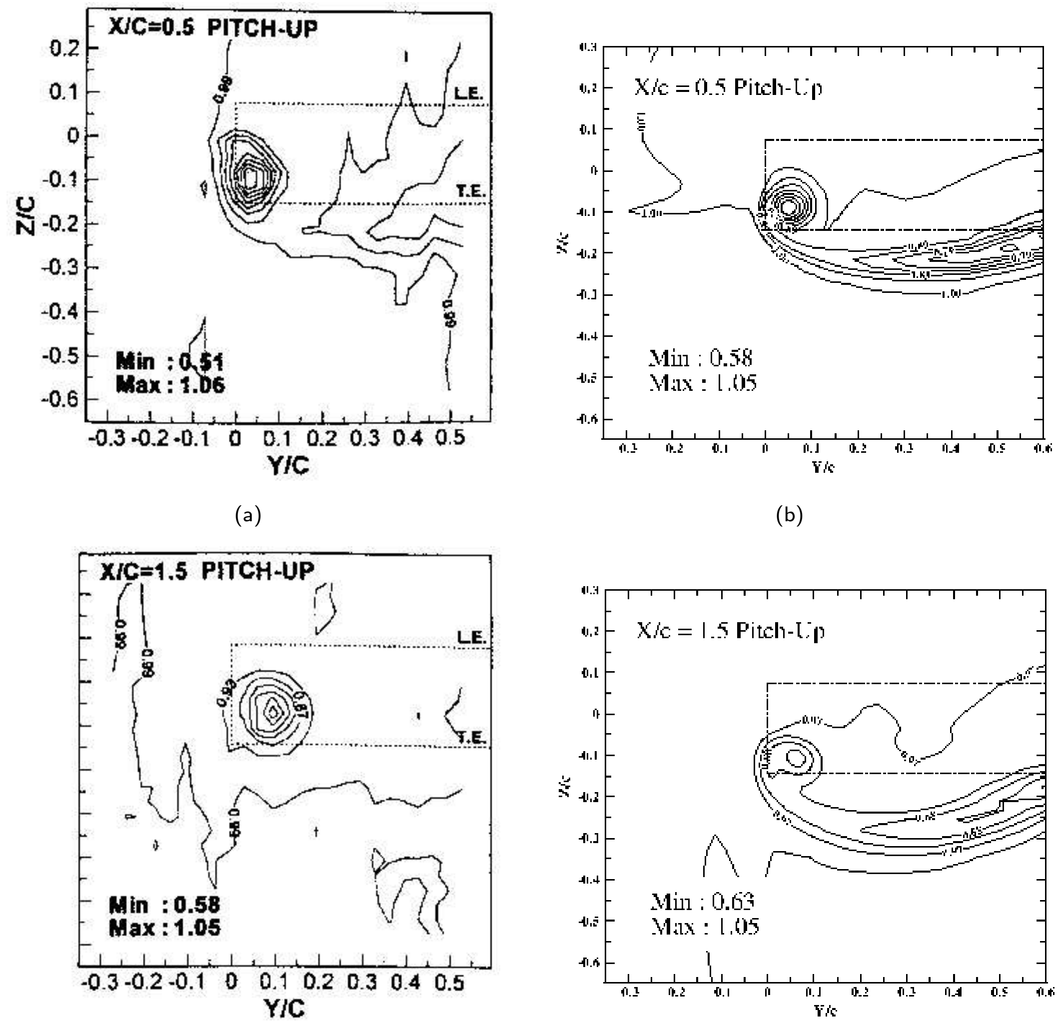

(a) (b) (c) (d)

Figure 8: Non-dimensional axial velocity in tip vortex from [10]. The conditions of the test correspond to the Test Case 3 reported in Table [3]. (a) experimental, (b) CFD, (c) experimental, (d) CFD.

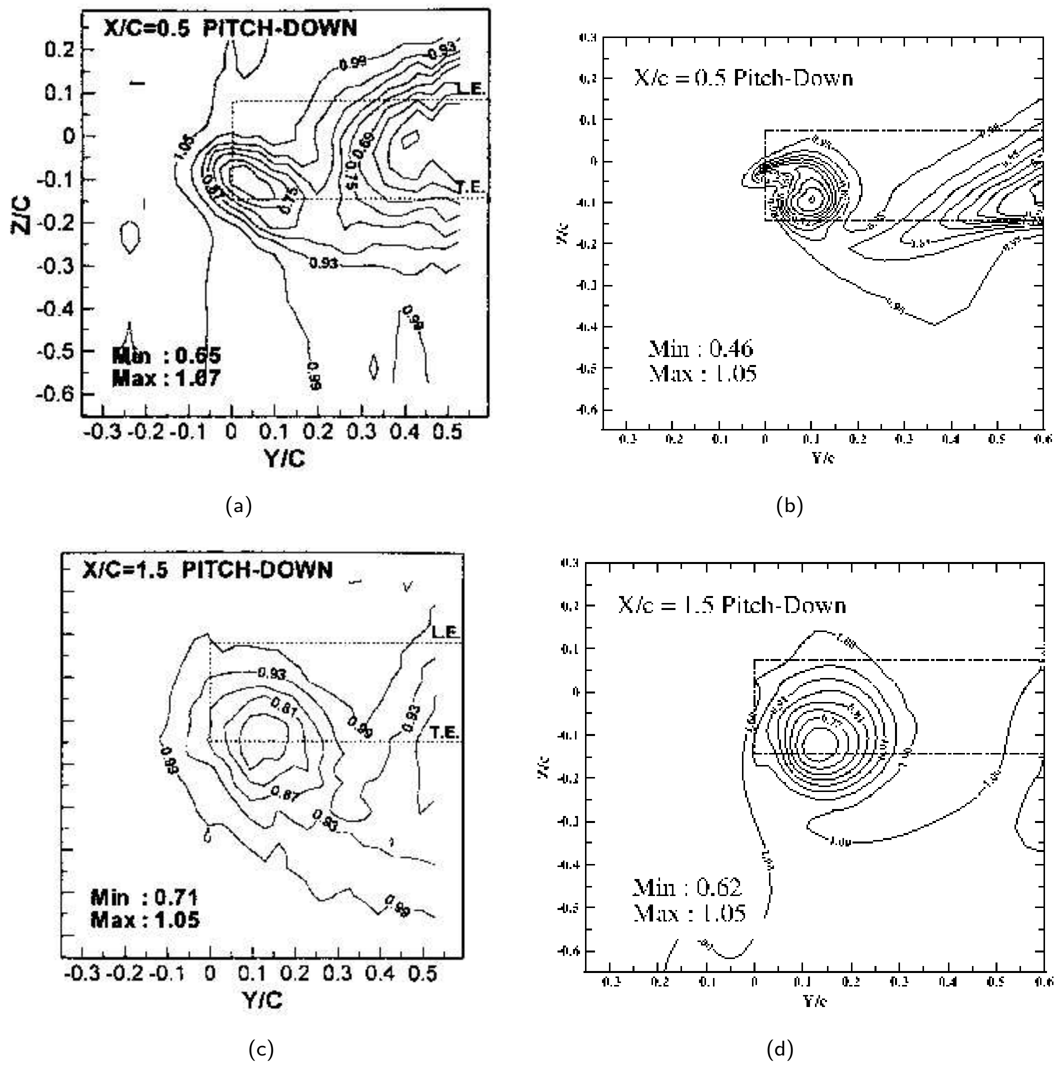

Figure 9: Non-dimensional axial velocity in tip vortex from [10]. The conditions of the test correspond to the Test Case 3 reported in Table [3]. (a) experimental, (b) CFD, (c) experimental, (d) CFD.

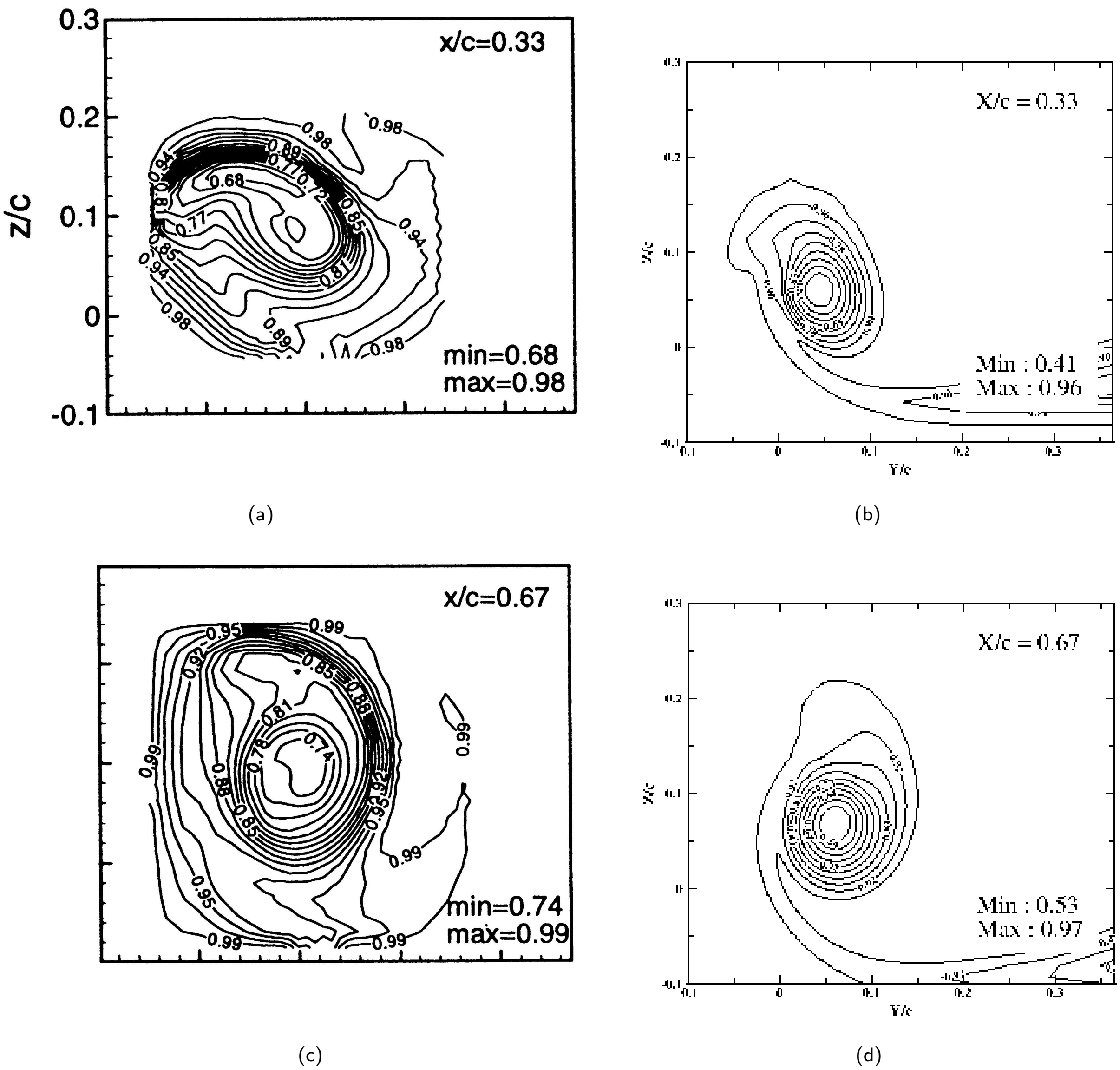

Figure 10: Non-dimensional axial velocity in tip vortex from [11]. The conditions of the test correspond to the Test Case 3 reported in Table [3]. (a) experimental, (b) CFD, (c) experimental, (d) CFD.

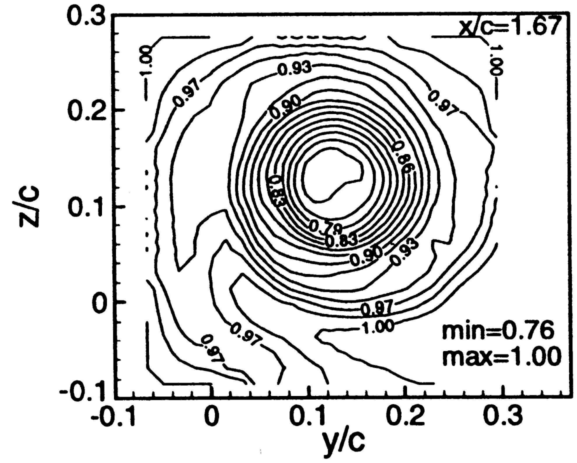

(a)

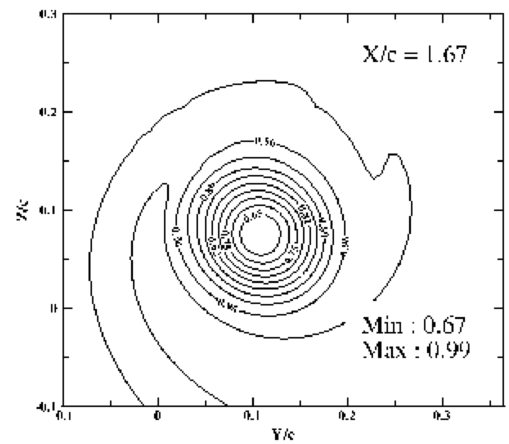

(b)

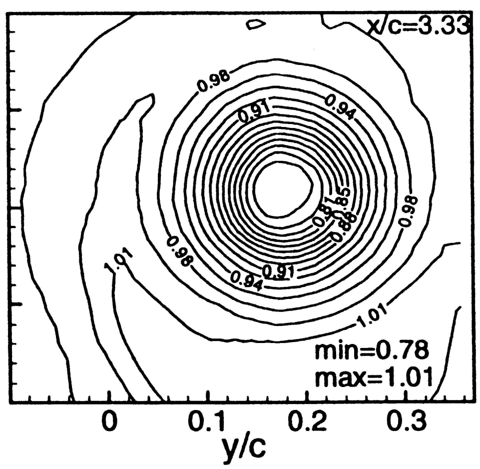

(c)

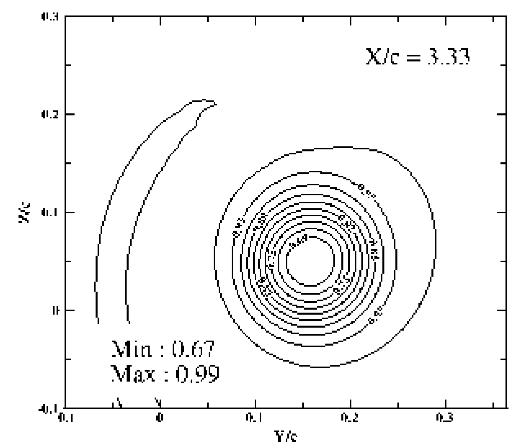

(d)

Figure 11: Non-dimensional axial velocity in tip vortex from [11]. The conditions of the test correspond to the Test Case 3 reported in Table [3]. (a) experimental, (b) CFD, (c) experimental, (d) CFD.

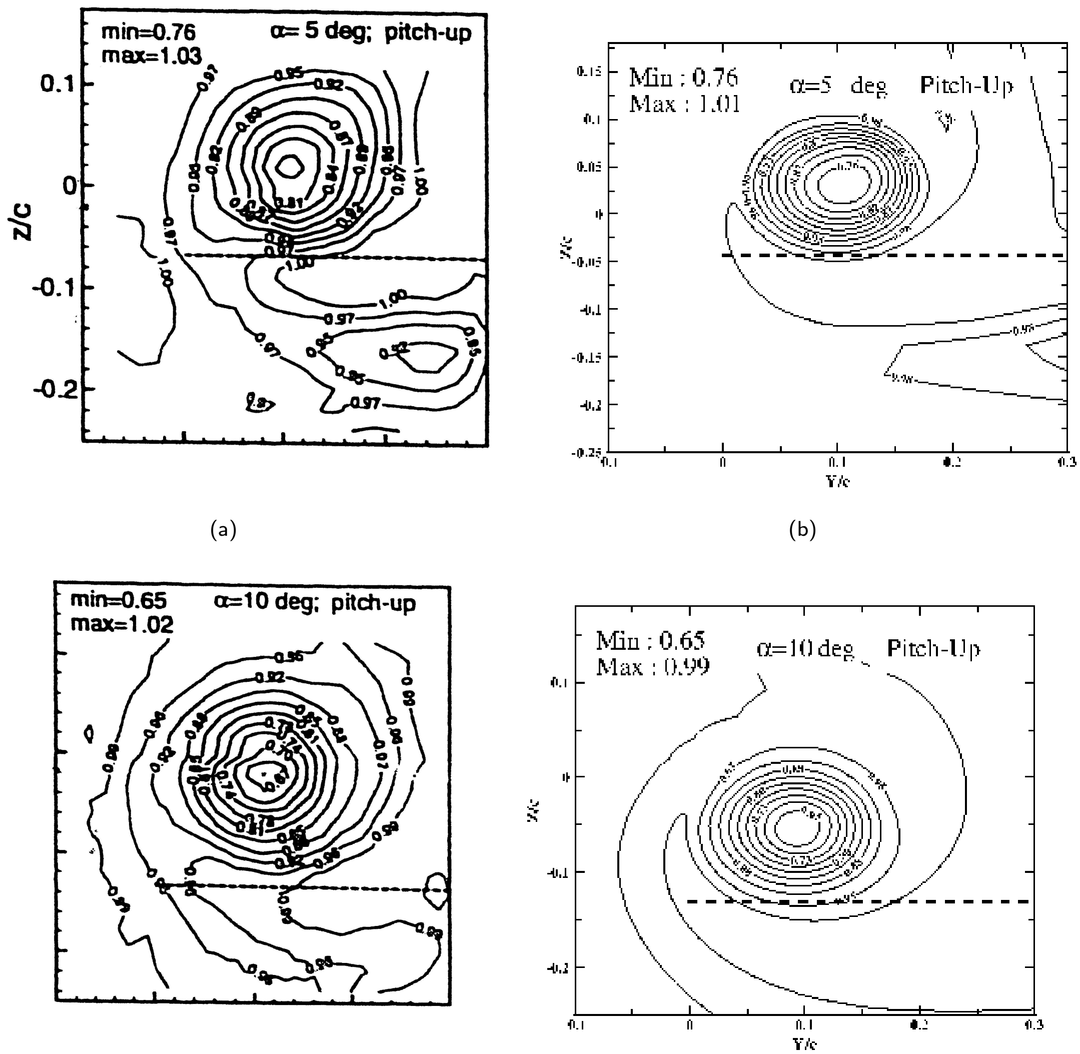

(a) (b)

(c) (d)

Figure 12: Non-dimensional axial velocity in tip vortex from [12]. The conditions of the test correspond to the Test Case 3 reported in Table [3]. (a) experimental, (b) CFD, (c) experimental, (d) CFD.

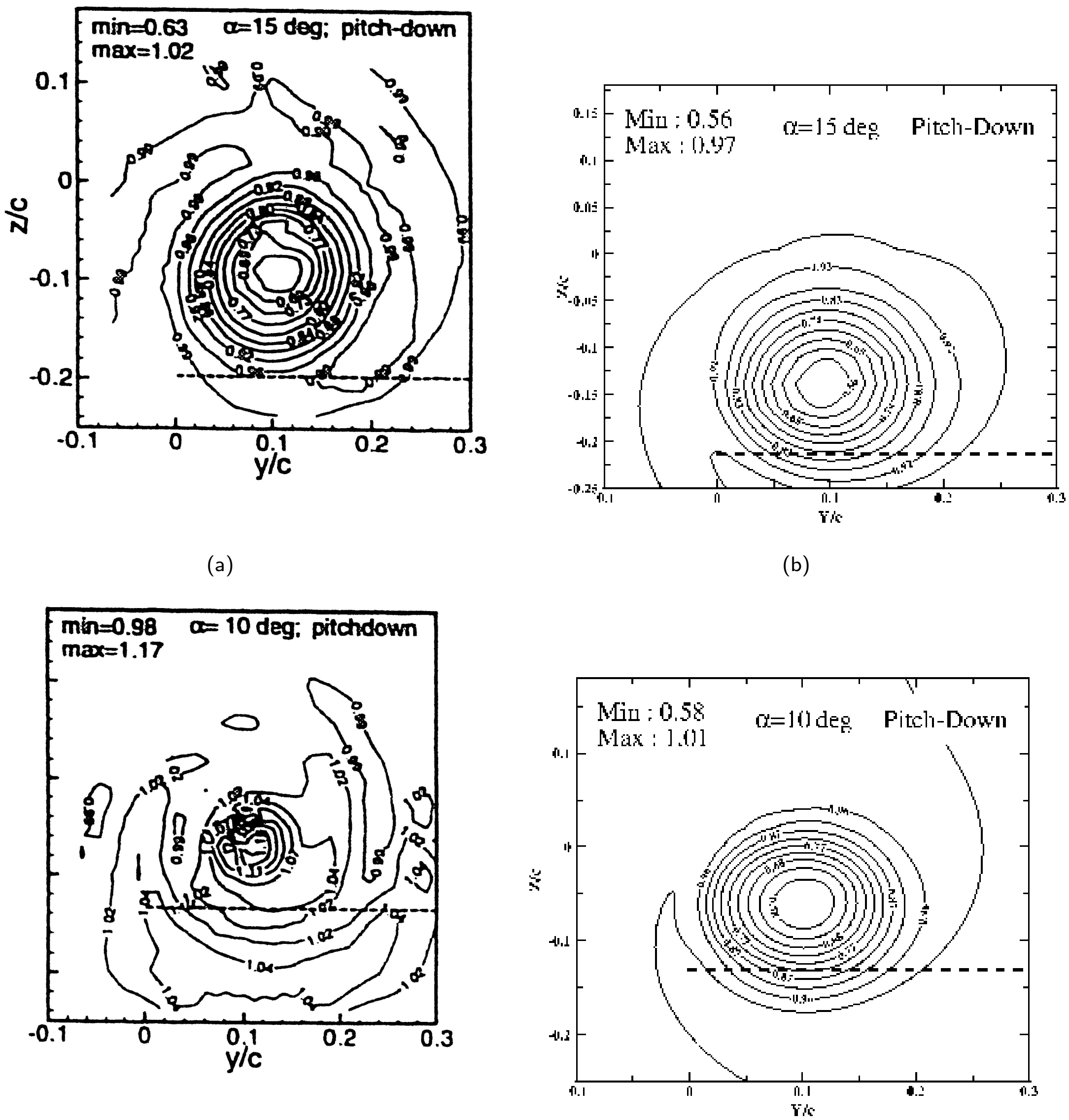

(c) (d)

Figure 13: Non-dimensional axial velocity in tip vortex from [12]. The conditions of the test correspond to the Test Case 3 reported in Table [3]. (a) experimental, (b) CFD, (c) experimental, (d) CFD.

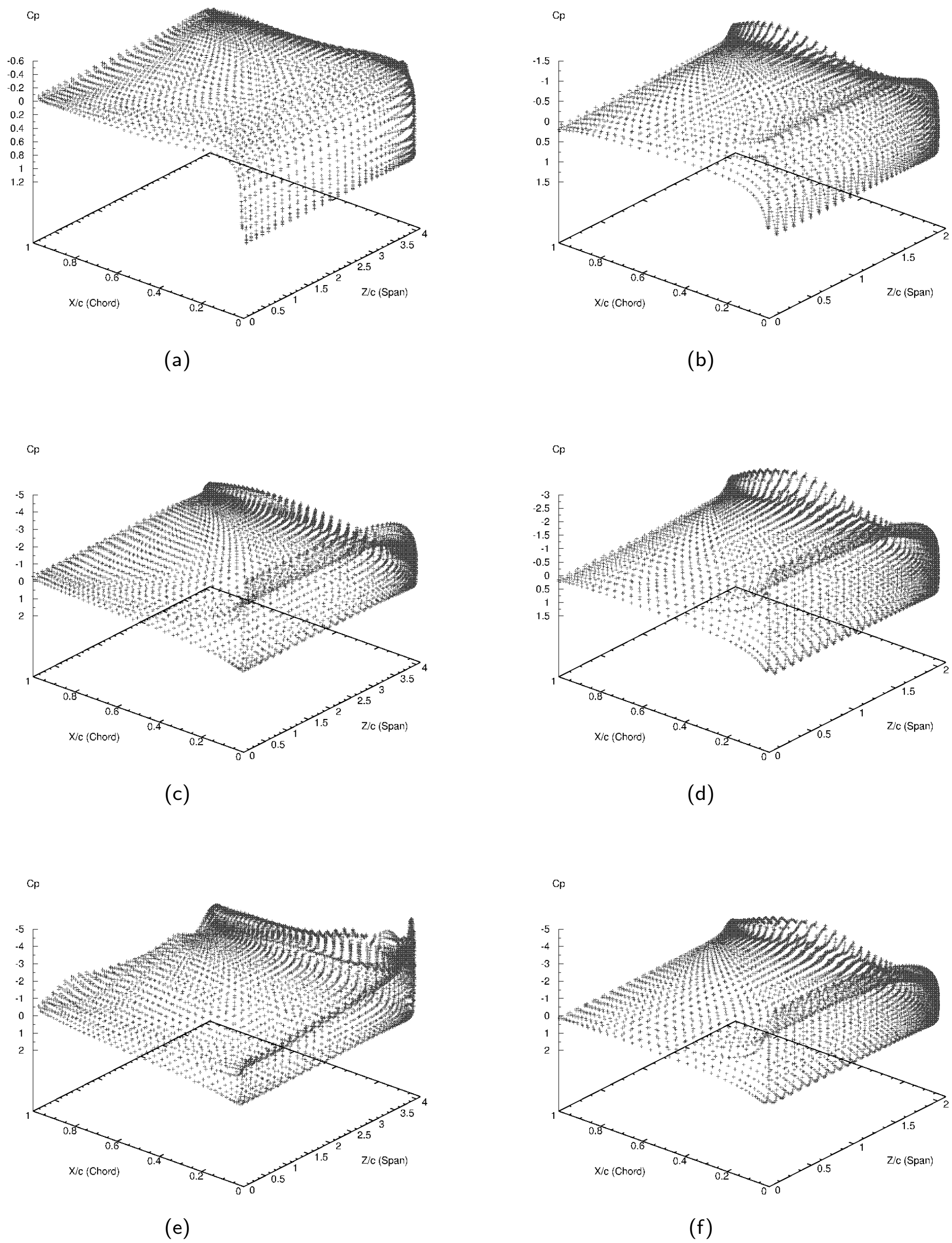

Figure 14: CFD results for the surface C_P variation for (a) $\alpha = 0$ *deg*, (c) $\alpha = 15$ *deg*, (e) $\alpha = 30$ *deg* during pitch-up. The conditions correspond to the experiments of Chang *et al.* [10] (see Test Case 1 in Table [3]), (b) $\alpha = 5$ *deg*, (d) $\alpha = 10$ *deg*, (f) $\alpha = 15$ *deg* during pitch-up. The conditions correspond to the experiments of Ramaprian *et al.* [12] (see Test Case 3 in Table [3]).